Published in final edited form as:
Ann Biomed Eng. 2014 February ; 42(2): 280–298. doi:10.1007/s10439-013-0895-2.

A physiological perspective on the use of imaging to assess the *in vivo* delivery of therapeutics

Shengping Qin, PhD[*],
Department of Biomedical Engineering, University of California, Davis

Brett Z. Fite, PhD[*],
Department of Biomedical Engineering, University of California, Davis

M. Karen J. Gagnon, PhD,
Department of Biomedical Engineering, University of California, Davis

Jai W. Seo,
Department of Biomedical Engineering, University of California, Davis

Fitz-Roy Curry, PhD,
Department of Physiology, University of California, Davis

Frits Thorsen, PhD, and
The Department of Biomedicine, Molecular Imaging Center, University of Bergen, Norway

Katherine W. Ferrara, PhD
Department of Biomedical Engineering, University of California, Davis

Shengping Qin: spqin@ucdavis.edu; Brett Z. Fite: bzfite@ucdavis.edu; M. Karen J. Gagnon: mkgagnon@ucdavis.edu; Jai W. Seo: jwseo@ucdavis.edu; Fitz-Roy Curry: fecurry@ucdavis.edu; Frits Thorsen: Frits.Thorsen@biomed.uib.no; Katherine W. Ferrara: kwferrara@ucdavis.edu

Abstract

Our goal is to provide a physiological perspective on the use of imaging to optimize and monitor the accumulation of nanotherapeutics within target tissues, with an emphasis on evaluating the pharmacokinetics of organic particles. Positron emission tomography (PET), magnetic resonance imaging (MRI) and ultrasound technologies, as well as methods to label nanotherapeutic constructs, have created tremendous opportunities for preclinical optimization of therapeutics and for personalized treatments in challenging disease states. Within the methodology summarized here, the accumulation of the construct is estimated directly from the image intensity. Particle extravasation is then estimated based on classical physiological measures. Specifically, the transport of nanotherapeutics is described using the concept of apparent permeability, which is defined as the net flux of solute across a blood vessel wall per unit surface area of the blood vessel and per unit solute concentration difference across the blood vessel wall. The apparent permeability to small molecule MRI constructs is accurately shown to be far larger than that estimated for proteins such as albumin or nanoconstructs such as liposomes. Further, the quantitative measurements of vascular permeability are shown to facilitate detection of the transition from a pre-malignant to a malignant cancer and to quantify the delivery enhancement resulting from interventions such as ultrasound. While PET-based estimates facilitate quantitative comparisons of many constructs, high field MRI proves useful in the visualization of model drugs within small lesions and in the evaluation of the release and intracellular trafficking of nanoparticles and cargo.

[*]Contributed equally to the paper.

Introduction

We imagine a future in which the earliest signs of disease are detected and progression is preempted. In this vision, imaging instruments detect small biochemical foci and targeted particles are introduced to selectively treat these lesions. The optimized particles are engineered for automatic release due to local endogenous conditions or activation by exogenous energy sources. These targeted and activatable nanoparticles can provide the potential for a leap in therapeutic efficacy, but will only succeed if circulation time, targeting, release and cellular internalization are co-optimized for *in vivo* efficacy. Historically, many carrier approaches have seemed promising *in vitro* only to fail as a result of a host of unforeseen mechanisms *in vivo*. Further, a rate limiting step within the pipeline of many potentially paradigm-changing nanotherapies is the lack of efficient means to obtain rapid and accurate quantitative pharmacokinetic data. As a result, off target effects can be easily missed and it is difficult to carefully compare the stability, biodistribution, targeting efficacy and route of injection for each particle. Therefore, we explore the development of techniques to image and optimize drug carriers *in vivo*. Our paper summarizes the perspective on image-guided delivery that was presented at the Frontiers in Bioengineering meeting held at the Georgia Institute of Technology in 2013 and is set in the context of the current state of image-guided delivery. Our goal is to bridge classical physiological analyses with state of the art imaging and to provide examples of the information that can be gained through quantitative imaging.

In many current human protocols, the percentage of the injected dose reaching a known solid tumor is very low, often less than 0.1% [29, 95]. By encapsulating hydrophilic and amphipathic drugs, a 300-fold increase in the area under the curve can be achieved, in addition to a great reduction in toxicity [39, 77], thus overcoming challenges in the systemic circulation of therapeutics (Fig. 1 left panel). A hydrophilic polymer coating, such as that obtained with polyethelene glycol, can also enhance systemic circulation of a particle. Further, nanoparticle drug delivery has the potential to eliminate the need for toxic diluents (e.g., Cremophor EL for paclitaxel) [60]. Yet, the nanocargo must become bioavailable in order for the therapeutic to be effective; this requires both tissue extravasation (Fig. 1 middle panel) and cellular internalization and trafficking (Fig 1 right panel). The addition of heat or pH activation technologies to enhance the extravasation of the particle or to release the cargo can further improve efficacy [3]. Here, we focus primarily on the use of imaging to quantify the circulation and extravasation of nanotherapeutics.

Many classes of nanotherapeutics have been synthesized or formulated, including lipid vesicles, polymeric shells and micelles, inorganic shells and particles and protein or peptide-based carrier systems. Each class of nanotherapeutic can be loaded with a vast range of cargo and targeted to specific cell surface receptors. Therefore, the potential design space is vast. For biological therapeutics, nanoparticle-mediated delivery may be particularly important because of its potential to deliver cargo to intracellular targets.

In addition, many newly identified molecular targets are accessible to small particles [44, 92, 109], including integrins, aminopeptidase A and N, nucleolin, neuropilin-1, inflammatory markers, and organ-specific receptors. Currently, the biodistribution of ligands targeted to these receptors has been characterized in only a few cases and particle targeting is even more poorly characterized. The targeting of particles is very different from small molecules, and, as a result, maintaining specificity is challenging.

With unique light scattering and photothermal properties and facile conjugation to biomolecules, inorganic nanoparticles (e.g. gold nanoparticles (GNPs) and modified gold nanoparticles) have emerged as promising optical imaging probes and drug carriers. The

optical properties of GNPs are governed by the localized surface plasmon resonance that depends on particle shape, size and dielectric property of the interface of the particle with the medium[21]. For GNPs, the plasmon resonance frequency and the light scattering lie in the visible NIR region of the electromagnetic spectrum[119]. Combining capabilities for controlling particle size and composition with versatile surface chemistry has led to optically and chemically reactive nanoparticle probes. Numerous GNP-based assays have been developed for the detection of targets such as metal ions, small organic compounds, nucleic acids, proteins and cells and have been reviewed recently[2, 4, 73, 80, 105, 119]. Here, we focus on organic nanoparticles in order to provide a physiological perspective to the use of imaging in tracking common drug delivery vehicles, including liposomes. We first summarize the use of imaging technologies to label and track therapeutic organic constructs, with a particular emphasis on positron emission tomography (PET) due to the sensitivity and flexibility of PET in characterizing a range of constructs. Next, we focus on the estimation of apparent permeability, defined as the net flux of solute across a blood vessel wall per unit surface area of the blood vessel and per unit solute concentration difference across the blood vessel wall, under the assumption of a nonzero flux of fluid across the wall. Such a measure provides a quantitative means to compare the accumulation and clearance within target tissues. The use of whole body imaging techniques to detect cargo internalization and trafficking is briefly described. Finally, we conclude with a discussion of future technologies and opportunities.

Use of imaging technology to quantify therapeutic delivery

The development of imaging methods to track therapeutic constructs is useful for the optimization of the pharmacokinetic and pharmacodynamic profiles. Image guidance methods using magnetic resonance imaging (MRI), ultrasound, and X-Ray computed tomography (CT) are well-known [8, 16, 50, 65, 130] (Table 1). Overall, the strengths of PET and other nuclear medicine techniques include high sensitivity, the opportunity to quantify accumulation and kinetics, the availability of a wide range of functional probes and the opportunity to tag therapeutic cargo with a radioisotope without altering fundamental properties of the material. Advantages of MRI include the wide range of physiological studies that can be performed using endogenous contrast agents, enhanced spatial resolution and the opportunity for activatable probes. Ultrasound also provides the opportunity to activate therapeutic carriers and to enhance the accumulation of therapeutics.

Magnetic resonance imaging

MRI routinely provides anatomical or functional detail of lesions in relation to surrounding tissues. In order to enhance the image contrast and detect disease at an early stage, multiple MRI contrast agents have been formulated. The purpose of a contrast agent is to locally alter the T1 or T2 time constants that are used within MRI imaging, in order to achieve a hyper or hypointensive signal in a short time. Gadolinium-based contrast agents (such as Omniscan™, OptiMARK™, Magnevist®, ProHance®, Dotarem® and MultiHance®) are the most commonly administered contrast agents in clinical MRI due to the high relaxivity, low toxicity, good solubility, low osmolality and high thermodynamic stability. Gadolinium-based MRI contrast agents that have been approved by the FDA have molecular weights on the order of 1 kDa. These contrast agents have been shown to distribute in vascular and extravascular spaces with few side effects [123]. Two iron-based nanoparticle contrast agents (Feridex® and Resovist®) are also approved. Of the two, Resovist® can be used in dynamic imaging studies, although the use is typically restricted to imaging hepatic lesions [118]. For the MRI analysis below, we focus on gadolinium-based agents as they can be applied to track drug delivery vehicles.

Dynamic contrast-enhanced MRI (DCE MRI) adds the dimension of time to the anatomic image of conventional MRI. Quantitative analysis of a series of DCE T1-weighted images at a time resolution of <20 seconds per image can determine physiological parameters of the tissue vasculature and interstitial space [103]. After a bolus injection of a low molecular weight contrast agent, the dynamic signal vs time curve, *S(t),* is acquired for each region of interest. The rapidity of tumor uptake of contrast agents and the rate of clearance of the agents from a tumor can be quantified and used to detect tumor malignancy and anticancer treatment response [30, 31].

MRI-based direct visualization of a drug released from a therapeutic carrier was first shown with temperature sensitive liposomes which contained manganese (II) [84]. Alternatively, liposomes labeled for detection via chemical exchange saturation transfer have been used to track liposomes and to detect the release of the cargo or the internalization of the entire particle [62, 104].

While therapeutic ultrasound can be applied to enhance accumulation under the guidance of ultrasound imaging, systems combining MRI and ultrasound (known as MR-guided focused ultrasound or MRgFUS) frequently have been applied to guide local drug delivery. Systems combining PET and MRI have been developed but applications are still emerging [56, 72] (Fig. 2). While PET allows us to visualize the accumulation of the injected radiotracer, MRI provides a three dimensional anatomical reference, can estimate the tissue temperature, can detect drug release and further can be used to assess the changes in tissue properties that result from the application of ultrasound [42, 49]. The most common implementations of MR thermometry use the temperature sensitivity of the proton resonance frequency of water molecules [87]. The proton resonance frequency has a thermal coefficient that is nearly independent of tissue type (excepting adipose tissue) [82]. The advantages of MRgFUS as a form of image-guided therapy are augmented at higher magnetic field strengths with improved resolution of temperature as well as improved spatial resolution [82]. The quasi-linear increase in both effective signal-to-noise ratio and the proton resonance frequency temperature sensitivity with increasing field strength improve image quality and temperature precision at ultra-high field strengths (≥ 7T) [32]. MRgFUS has been demonstrated to provide the fine control of temperature required for mild hyperthermia (41–42 °C) as well as the ability to guide ablation[32, 78, 79, 89].

Positron Emission Tomography

PET and other nuclear medicine imaging methods have been applied to image the distribution and kinetics of peptides and antibodies, due to the opportunity to quantify accumulation and clearance relative to the injected dose. Given the vast literature concerning liposomal, micellar and polymeric formulations, quantitative imaging can play a key role in facilitating head to head comparisons of the delivery achieved with various constructs. For more than two decades, liposomes radiolabeled with either technetium-99m [6, 7, 9, 20, 63, 74, 75, 83] or gallium-67 [38, 74–76, 127] have been utilized as radiotracers for single photon emission computed tomography, with significant effort invested into minimizing the dissociation of the radiolabel from the particle. In order to utilize the superior sensitivity and resolution associated with PET, more recent efforts have focused on developing radiotracers containing positron emitting nuclides such as copper-64 (Cu-64) [100, 114], fluorine-18 (F-18) [110] or zirconium-89 (Zr-89) [23]. While liposomes radiolabeled with F-18 ($t_{1/2}$=109.7 min) via incorporation of ^{18}F]fluorodipalmitin into the lipid bilayer have proven useful [70, 77, 133], the short half-life of F-18 makes extended studies difficult.

Since it is desirable to create stable particles that can circulate and accumulate in tumors over days to weeks, Cu-64 is applied in imaging, as it has a longer half-life ($t_{1/2}$=12.7 hrs)

and can be incorporated via either a surface chelation method [97] or through the use of a bifunctional chelator [96]. The surface chelation method (Fig. 3 panel A) has proven to be a flexible method for incorporating Cu-64 onto liposomes [97]. In this approach, the chelator-lipid (6-[*p*-(bromoacetamido)benzyl]-1,4,8,11-tetraazacyclotetradecane-*N*,*N*′,*N*″,*N*‴-tetraacetic acid (BAT)-PEG-lipid) is incorporated during initial particle formation; Cu-64 is then captured by the chelator on the surface of the fully assembled liposome. Using this approach, liposomes have been labeled with Cu-64 for imaging murine models of carcinoma [93, 125], as well as achieve dual imaging with a near infrared dye to evaluate the pharmacokinetics of drug release *in vivo* [77, 86, 97]. Alternatively, a bifunctional chelator can be used wherein (6-(6-(3-(2-pyridyldithio)propionamido)hexanamido) benzyl)-1,4,8,11-tetraazacyclotetradecane-1,4,8,11-tetraaceticacid (TETA-PDP) or 4-(2-(2-pyridyldithioethyl)ethanamido)-11-carboxymethyl-1,4,8,11-tetraazabicyclo(6.6.2)hexadecane (CB-TE2A-PDEA) are radiolabeled independently and then incorporated onto the surface of the already formed liposome (Fig. 3 panel B). This flexible post-labeling approach is not restricted to lipids and may also hold application for labeling block-copolymers, iron oxide nanoparticles, quantum dots and gold nanoparticles. In both approaches, the *in vivo* stability of Cu-64 chelated to TETA or BAT was similar to that of the cross-bridged chelator TE2A [96].

In order to further extend the use of liposomes in imaging, Zr-89 ($t^{1/2}$ = 78.4 h) has been incorporated onto the surface of liposomes using a chelator-free labeling concept [1]. This report showed that ^{89}Zr oxophilicity results in reasonable stability for chelator-free liposomes in the presence of serum proteins.

Micelles are also of interest due to the smaller diameter of many formulations and the potential to carry hydrophobic drugs. Micelles containing drugs such as cisplatin [24, 64, 117], paclitaxel [17, 24, 64] and doxorubicin [54, 122, 129] have been reported. In these examples, micelles have been evaluated either in vitro or labeled with a fluorochrome for optical imaging; in order to utilize micelles for PET imaging a radiolabel must be incorporated into the micelle. As with liposomes, the surface chelation method provides a straightforward approach for the radiolabeling of micelles. Again, the chelator-lipid is incorporated at the time of particle formation and the fully assembled particle is radiolabeled with Cu-64 (Fig. 3 panel C). Micelles radiolabeled with Cu-64 and loaded with doxorubicin have been used to evaluate circulation kinetics, accumulation, targeting and clearance in a murine model of breast cancer [27]. Similarly, radiolabeled micelles containing targeting ligands on the surface have been used for evaluating cell uptake, biodistribution and tumor retention in murine models of carcinoma [91], as well as evaluating the pH-controlled drug release of covalently attached doxorubicin in murine models of glioblastoma [128].

Radiolabeled monoclonal antibodies, or engineered antibody fragments such as nanobodies [25, 94], are broadly used for *in vivo* research to understand biological processes, as well as for the treatment of systemic diseases such as cancer. ImmunoPET (using antibodies for PET imaging) combines the advantages of PET with the specificity of antibodies. Antibodies have been radiolabeled with a variety of radioisotopes; antibodies radiolabeled with Zr-89 using DFO-based conjugation strategies are of particular interest since the circulation half-life of 2–4 days for typical intact antibodies is complementary to the long half-life of Zr-89 [112, 135]. Recent reports have illustrated the use of ^{89}Zr-labeled antibodies for imaging human epidermal growth factor receptor 1 (HER-1) expressing carcinomas *in vivo* [11], imaging CD147 expression in a murine model of pancreatic cancer [101] and evaluating ^{89}Zr-labeled epidermal growth factor receptor (EGFR)-targeted antibodies *in vitro* and *in vivo* [15].

Peptides have garnered interest as molecular imaging agents for the targeting of a variety of diseases and have been radiolabeled for many years. Peptides are attractive since their relatively small size results in high target-to-background ratios due to their rapid targeting and blood clearance *in vivo*. Peptides have been radiolabeled with Cu-64 [66, 98, 99, 113] via chelation strategies similar to those outlines above; however, due to the rapid clearance of peptide based radiopharmaceuticals *in vivo* there has been little need to radiolabel with longer lived isotopes such as Zr-89 [53]. In contrast, a large number of peptides have been radiolabeled with F-18 and evaluated *in vivo* using PET [43, 45, 67, 81, 134]. One approach to radiolabeling peptides with F-18 is through on-resin coupling of the peptide with ^{18}F-fluorobenzoic acid ([^{18}F]FBA), followed by cleavage and purification to give the desired ^{18}F-radiolabeled peptide (Fig. 3 panel D) in high radiochemical purity and with high specific activity [124]. This approach has proven to be highly robust and reliable, allowing for the development of a high-throughput screening technique for the identification of peptide-based targeted molecular imaging agents [40].

Enhanced delivery with ultrasound

The thermal and mechanical effects of ultrasound have been recognized as impacting tissue properties for many years, with the earliest effects detected in the central nervous system [34–36, 69, 115]. High intensity ultrasound was recognized to produce lesions in tissue in 1942 and has been applied to ablate tissue, enhance drug delivery and induce a systemic immune response.

There are multiple mechanisms by which ultrasound can enhance drug penetration. Typical *thermal* strategies employ either high temperature ablation or mild hyperthermia to increase drug accumulation within the lesion and lesion boundary. In such strategies, the increased temperature can influence both the tissue and the drug capsule. Alternatively, the *mechanical* effects of ultrasound can act directly upon the tumor tissue or on injected microbubbles whose oscillations enhance vascular or cell membrane permeability. There have been numerous reports of enhanced extravasation of antibodies and nanotherapeutics as a result of direct effects of ultrasound on tissue and vasculature although the mechanisms are still under investigation [33, 116, 120]. For example, when a train of 100 pulses of 1 MHz ultrasound at a peak negative pressure of 8.95 MPa and duty cycle of 5% were applied to tumors, antibody penetration was reported to be significantly enhanced at the tumor periphery through mechanical effects [116].

Thermal dose is typically estimated as cumulative equivalent minutes at 43°C (CEM 43), which is defined as $tR^{(43-T)}$, with t being the time of treatment, T the average temperature during treatment, and R a constant that equals 0.25 for temperatures between 37 and 43°C and 0.5 above 43°C [26, 55]. When the tissue temperature exceeds 60°C and a sufficient thermal dose is achieved, the resulting tissue ablation also enhances drug and nanoparticle accumulation. RF ablation has been applied in previous studies to achieve a similar enhanced delivery and such techniques are now in clinical trials [41, 126]. High intensity ultrasound similarly enhances delivery surrounding the site of ablation, although this combined technique remains under investigation in pre-clinical studies. Mild hyperthermia (CEM 43 <0.5) is associated with increased metabolism, blood flow and tissue repair. Higher thermal doses are associated with enhanced cell death [90]. Hyperthermia has additional benefits to drug delivery, with increased accumulation as a consequence of increased tumor blood flow and increased microvascular permeability [37]. Unlike strategies which use microenvironment-sensitive activation mechanisms, hyperthermia is limited to use in tumors of known location and reasonable accessibility.

Image-based pharmacokinetics

Many imaging modalities have been utilized to extract pharmacokinetic data including PET, MRI, x-ray CT and optical methods. Recent work has suggested parity in image derived parameters between DCE-CT and DCE-MRI [59]. The wide availability of CT scanners and the linear relationship between the signal change and the contrast agent concentration are strong motivating factors for the use of CT. However, radiation dose is a major limiting factor especially when the late phase kinetics is of interest or when repeated examinations are desired. Moreover, MRI may provide a better anatomical context to contrast agent kinetics when soft tissue comprises the majority of the tumor or tissue of interest.

For organic nanoparticles, optical methods are particularly useful in tracking the particle cargo and can provide an activatable signal that changes with cellular uptake and trafficking [77]. Methods to integrate full body pharmacokinetics using PET, MR or CT with cellular uptake and trafficking using optical probes will be important extensions but have not yet been fully developed, although multiple groups have developed dual modality particles incorporating an optical probe.[57] With a primary focus on the application of imaging for the evaluation of system level pharmacokinetics, in the following sections we will summarize the pharmacokinetic approaches using MRI and PET.

PET and MRI images have been used to quantify the pharmacokinetics and transport of small molecules for many years; however, the application of imaging to assess the transport of macromolecules and nanotherapeutics is still emerging (Fig. 4a). Practically, the data acquisition is far different; to characterize the dynamics of small molecular weight agents, the kinetics must be quantified as the injected bolus equilibrates and clearance can be expected to occur within tens of minutes. Alternatively, for macromolecules or nanotherapeutics with an extended circulation half-life, images acquired at the time of injection may not provide useful data, since the initial volume of distribution is approximately limited to the blood pool. Images must be acquired over many hours or days to fully characterize the time course of distribution and clearance.

Classical approaches for image-based pharmacokinetic models

Compartmental modeling is considered to be most accurate method to analyze PET dynamic data and is therefore used as a “gold standard”; its application to the estimation of apparent permeability will be detailed below. The ability to quantify accumulation and account for attenuation has enhanced the use of PET for pharmacokinetic modeling. PET-MRI images facilitate the identification of the region of interest using MRI while the accumulation of the therapeutic is visualized with the PET image (Fig. 4a). Both one and multi-compartment models have been created, with the kinetic parameters considered to be equal or differing in each direction and accumulation modeled as reversible or irreversible (Fig. 4b–d) [108].

For small molecule tracers, various quantitative methods have been proposed in clinical PET practice as well as in oncology research. The standard uptake value is the most widely used parameter for clinical analysis of radiotracers because of the short scan time required for most tracers and the reduced computational complexity. Standard uptake value is defined as the ratio between radiotracer concentration in a region of interest and the normalized injected activity. Three normalization factors are commonly used: body weight (kg), body surface area (m^2) and lean body mass (kg) [108]. However, the main pitfall of the standard uptake value is that the derived values often cannot be compared across different centers [13, 108, 121].

Graphical methods, such as the Patlak plot and the Logan plot, allow for calculation of the uptake rate of the radiotracer in the tumor compartment at a given time after the

administration of the radiotracer (the required delay depends on the specific tracer properties). The Patlak plot derives the irreversible uptake rate at which the tracer is trapped in the region of interest by linearly fitting the ratio of the tissue time activity curve and plasma time activity curve versus the ratio of the time integral and the instantaneous values of the plasma time activity curve. The Logan plot is the counterpart of the Patlak plot for reversible tracers. Equations from Patlak and Logan plots are linear and computation is fast and robust [68]. We have applied these tools to quantify the accumulation of targeted liposomes to the vasculature of the heart, demonstrating that such particles accumulate within tens of seconds [132]. The Logan plot has been used to demonstrate the difference in volume of distribution between targeted particles with an exposed, as compared with a buried, ligand [132].

Here, we focus on the application of imaging data and compartmental models to characterize the bidirectional transport of therapeutics between the blood pool and the interstitium of the target tissue, frequently cancerous tumors (Fig. 4) [108]. Such models are based on classical physiological parameters.

Assessment of apparent vascular permeability and other classical physiological parameters

We first detail the relationship between classical parameters (apparent permeability, solute transport coefficient, clearance, and 30 minute clearance) and the parameters derived through the image-guided model. The net flux of solute J_S across a blood vessel wall can be described by the Kedem – Katchalsky equation:

$$J_S = P_d S \Delta C + J_V (1-\sigma_f) C_S \quad (1)$$

where P_d is the microvascular diffusive permeability, S is the total surface area of the blood vessel, J_V is the net flux of fluid, σ_f is the filtration reflection coefficient, ΔC is the solute concentration difference cross the blood vessel wall and C_S is the average solute concentration within the blood vessel.

Permeability under the assumption of equal transport into and out of the region (Fig. 4b)

Because the net flux of fluid, J_V, cannot be measured directly and is not typically known, the apparent permeability (P_{AP}) for the combined convective and diffusive effects has been introduced as [28, 86]:

$$P_{AP} = \frac{J_S}{S\Delta C}\Big|_{J_V \neq 0} \quad (2)$$

Although J_v is not usually measured, some estimates of the contribution of convective transport can be made. For example, a trans-vascular pressure difference as small as 1 cm H_20 will result in a trans-vascular water flow of the order $2–10 \times 10^{-8}$ cm/sec across the walls of microvessels in normal organs such as skin and muscle, with higher values in leaky microvessels. When the ratio of filtrate to plasma concentration (known as the sieving coefficient and equal to $(1- \sigma_f)$) is close to 0.1 and the apparent permeability is on the order of 2×10^{-8}cm/sec, the convective component of transport of solutes such as albumin may account for 10–50% of the measured trans-vascular solute flux. When permeability is increased, the sieving coefficient may approach 1 (e.g. in the presence of a few large pores with increased water conductivity and σ_f close to 0) and the convective transport may be dominant in the direction of flow. A similar conclusion applies with an increased blood to

tissue pressure difference. Conversely, transport against net filtration (e.g. tissue to blood) may be significantly reduced in such cases.

Solute Transport Coefficient

Based on Eq. 2, we previously proposed an imaging-driven pharmacokinetic model for nanotherapeutics which simultaneously incorporates the kinetics of encapsulated drugs and delivery vehicles with the assumption that the solute transport rate depends on the solute concentration difference across the blood vessel wall [86]. A separate compartment was designed for the reticuloendothelial system to describe the metabolic processes for the delivery vehicles and the elimination of the metabolites from the blood pool. Because of the rapid clearance of the metabolites, without loss of generality, we simplify the model here to a two compartment model (Fig. 4b) to describe the pharmacokinetics of the delivery vehicle. The governing equations can be written as:

$$\frac{dC_P}{dt} = -k_e C_P - \lambda \frac{V_T}{V_P}(C_P - C_T) \quad (3a)$$

$$\frac{dC_T}{dt} = \lambda (C_P - C_T) \quad (3b)$$

where the subscripts *P* and *T* denote the plasma compartment and extravascular-extracellular (interstitial) tumor compartment, respectively; C_i is the solute concentration in compartment *i;* V_i is volume of distribution in compartment *i*; and k_e is the solute elimination rate through the kidney. λ is the solute transport constant across the vessel wall, which is defined as total solute flux per unit extravascular-extracellular tumor volume and per unit concentration difference across the vessel wall. Using our notation, λ is equivalent to the rate constant k_{ep} in the ratio of K^{trans} and the extravascular-extracellular volume fraction. K^{trans} is the volume transfer constant between the blood plasma and extravascular-extracellular space used within MRI pharmacokinetic analyses [106]. λ can be expressed as:

$$\lambda = \frac{J_S / V_T}{\Delta C}\Big|_{J_V \neq 0} \quad (4)$$

Eqs. 2 and 4 lead to:

$$P_{AP} = \lambda \frac{V_T}{S} = \frac{\lambda}{\eta}\frac{r}{2} \quad (5)$$

where *r* is the mean radius of blood vessels in the tumor and η is the plasma volume fraction in the tumor. η can be directly estimated from PET image data as described below and *r* estimated from histological data. Eqs. 2–5 can be further extended to define a time dependent solute transport rate, λ_3, which can be applied to evaluate the effect of interventions such as ultrasound.

Clearance

The apparent permeability (P_{AP}) can also be expressed in terms of the clearance (*Cl*) which is typically defined by J_S/C_S:

$$P_{AP}=\frac{J_S}{S\Delta C}=\left[\frac{\frac{J_S}{C_S}}{V_P}\right]\frac{V_P}{S}\frac{C_S}{\Delta C}\approx\left[\frac{\frac{J_S}{C_S}}{V_P}\right]\frac{V_P}{S}=\frac{Cl}{V_P}\frac{r}{2} \quad (6)$$

where $\frac{C_S}{\Delta C}\approx 1$ is assumed for the microenvironment and V_P is tumor plasma volume.

The 30 minute clearance (Cl_{30}) is an estimate of the volume of plasma that would contain the amount of tracer (ΔM_{30}) transported from the vascular compartment to the extravascular space in 30 minutes and can be used to validate image estimates of apparent permeability [19]. Thus, $Cl_{30}= \Delta M_{30} /C_s$. $J_s= \Delta M_{30}/1800$ sec and from Eq. 6:

$$P_{AP}=\frac{Cl_{30}}{1800\ sec}\frac{r}{2V_P}=\frac{Cl_{30}}{1800\ sec}\frac{r}{2\eta V_T} \quad (7)$$

Application of these principles in positron emission tomography

For PET tracers, the imaging intensity in the blood region of interest, $I_B(t)$ and tumor region of interest, $I_{Tm}(t)$ at time t can be quantified with units of percentage of the injected dose per cubic centimeter unit (%ID/cc). For macromolecular and nanotherapeutic PET analyses, the volume of distribution at time 0 can be approximated as the blood pool and therefore the plasma volume fraction can be estimated as shown below. Also, the cardiac chambers can be used to estimate the blood concentration of the tracer. Because of the linearity of Eqs. 3 (a) and (b), the concentrations of $C_P(t)$ and $C_T(t)$ can also be normalized by injected dose and thus have units of %ID/cc. For simplicity, we neglect correction for the extracellular volume fraction of the tumor, as this correction is not typically applied in PET analyses. Therefore we have the relationship:

$$I_B(t)=C_P^*(t)(1-Hct) \quad (8a)$$

$$I_{Tm}(t)=\eta C_P^*(t)+[1-\eta/(1-Hct)]C_T^*(t) \quad (8b)$$

where $C_P^*(t)$ and $C_T^*(t)$ are the normalized concentration in the plasma and tumor compartments with units of %ID/cc, and *Hct* is the hematocrit. For macromolecular and nanotherapeutic PET analyses, at the time of injection, we have conditions of $C_T^*(0)=0$ and $\eta=I_{Tm}(0)/C_P^*(0)$.

Combined with Eqs. 3–5, Eqs. 8a–b can be applied to predict $C_T(t)$ and to evaluate the apparent permeability and the accumulation of nanoparticle therapeutics in the tumor compartment. In Fig. 5a–d, the PET and optical images are shown and the intensity is plotted as a function of time after IV administration of the particles. Although methods for time dependent permeability analysis are not included here, our results indicate that an estimate of the time dependent solute transport rate in the insonified tumor, λ_3, is elevated by ultrasound for more than 10 hours as compared with a contralateral control (Fig. 5e).

We have examined the apparent permeability of long circulating liposomes (LCL), temperature-sensitive liposomes (TSL) and albumin in various tumor models, including syngeneic breast tumors, mouse mammary intraepithelial neoplasia outgrowths (MIN-Os), and epithelial and epithelial–mesenchymal transition tumors (EMT) [86, 93, 120]. Overall, the permeability is ~4 fold greater for albumin, as compared with 100 nm liposomes (Table 2). In each case, the permeability increases in the transition from a pre-cancer to a fully

developed cancer, with the permeability to albumin reaching 6.6×10^{-8} cm/s in the fully developed MIN-O tumor; also, the increase in permeability to albumin occurs earlier in the disease process than the change in permeability to liposomes (Table 2).

Apparent permeability was also shown to be ~50% greater in epithelial, as compared with epithelial-mesenchymal transition (EMT) breast cancer [120]. The Met-1 syngeneic mouse model of epithelial breast cancer is highly vascularized with large vascular sinuses at the tumor boundary, and with an apparently permeability to 100 nm liposomes of $4.1\pm2.8\times10^{-8}$ cm/s and $6.7\pm4.6\times10^{-8}$ cm/s before and after the application of ultrasound [120]. The apparent permeability for the EMT tumors, with their smaller vessel diameter and reduced vascular density was less than that of the epithelial tumors and increased significantly with ultrasound (Table 3). The optimal thermal dose and peak negative pressure were lower for epithelial, as compared with EMT, tumors, likely due to vascular stasis in the epithelial vasculature at the higher thermal dose. While mild hyperthermia enhanced accumulation in the epithelial tumors, likely through decreased intratumoral pressure and enhanced apparent permeability, higher ultrasound pressure was required to enhance delivery in the poorly vascularized EMT phenotype (Table 3).

Apparent permeability allowing for differences in transport into and out of the tumor

Eqs. 2~6 best describe scenarios where the diffusion process dominates the solute transport across the blood vessel wall such as the case of large solute particles, for instance liposomes, or for tissues in which convective transport can be neglected. In a number of scenarios (high intensity ultrasound, small tumor metastases and the transport of contrast agents with low molecular weight), evaluation of a time dependent permeability or separation of the transport coefficient into components into and out of the tissue is required to minimize errors. For simplicity and without loss of generality, the kinetics of solute concentrations into and out of a tumor can be separated as described by a two compartment pharmacokinetic model as in Fig. 4c. For reversible accumulation with the tumor, the resulting governing equations are:

$$\frac{dC_P}{dt}=k_{TP}\frac{V_T}{V_P}C_T-(k_{PT}+k_e)C_P \quad (9a)$$

$$\frac{dC_T}{dt}=k_{PT}\frac{V_P}{V_T}C_P-k_{TP}C_T \quad (9b)$$

where k_{ij} are the transport constants from compartment *i* to compartment *j*. As such, from Eq. 2, the apparent permeability can be defined as the agent flux across the blood vessel per unit surface area and per unit source concentration. The apparent permeability into the tumor can be written as:

$$P_{PT}=\frac{J_S}{S\,C_P}=\frac{J_S/V_P}{C_P}\frac{V_P}{S} \quad (10a)$$

and the apparent permeability out of the tumor is:

$$P_{TP}=\frac{J_S}{S\,C_T}=\frac{J_S/V_T}{C_T}\frac{V_T}{S} \quad (10b)$$

From Eq. 9(a), k_{PT} can be interpreted as the agent flux across the blood vessel per unit plasma volume and per unit concentration of C_P Therefore, we have $\frac{J_S/V_P}{C_P}=k_{PT}$ and Eq. 10(a) becomes

$$P_{PT}=k_{PT}\frac{V_P}{S}=k_{PT}\frac{V_P}{V_T}\left(\frac{r}{2\eta}\right) \quad (11a)$$

Similarly, Eq. 9(b), k_{TP} can be interpreted as the agent flux across the blood vessel per tumor volume and per unit concentration of C_T. Therefore, we have $\frac{J_S/V_T}{C_T}=k_{TP}$ and Eq. 10(b) becomes

$$P_{TP}=k_{TP}\left(\frac{V_T}{S}\right)=k_{TP}\left(\frac{r}{2\eta}\right) \quad (11b)$$

Modified permeability function

The derived apparent permeability in Eqs. 5 and 11 is intended to describe the fundamental permeability of the vessel wall to a particular construct. However, because the difference in the agent concentrations in the blood and tumor are substantial, the magnitude of the apparent permeability into and out of the tumor could differ by a few orders of magnitude, as each is normalized by the source concentration. Instead, the flux rate across the blood vessel (J_S) per unit surface area (S) can be applied to directly compare the transport into and out of the tumor. The modified apparent permeability into the tumor is linearly related to the agent concentration in the plasma (C_P):

$$P^*_{PT}=\frac{J_S}{S}=C_P k_{PT}\frac{V_P}{V_T}\left(\frac{r}{2\eta}\right) \quad (12a)$$

and that out of the tumor is linearly related to the agent concentration in tumors (C_T):

$$P^*_{TP}=\frac{J_S}{S}=C_T k_{TP}\left(\frac{r}{2\eta}\right). \quad (12b)$$

Extension of the model to MRI

In contrast to pharmacokinetic modeling with PET data, MR signal intensity has a more complex relationship with contrast agent concentration, as the data are a function of the particular imaging sequence, background signal, relaxivity of the contrast agent (itself a field dependent property), injected dose, and concentration of the injected bolus. Further, depending on the MR sequence selected, endogenous contrast mechanisms introduce a background signal that must be differentiated from the exogenous agent. In addition, the sensitivity of MRI to contrast materials is typically considered to be multiple orders of magnitude lower than PET. However, there are several fundamental advantages to the application of MRI in tracking model therapeutics. First, with high field MRI, the accumulation of constructs in small lesions can be assessed with spatial resolution that cannot currently be obtained with PET. Also, with gadolinium and chemical exchange saturation transfer agents, the MRI signal is sensitive to changes in the environment, and therefore it is feasible to differentiate extracellular and intracellular materials [104]. With

sufficient information, MRI pharmacokinetic models can provide reliable insight into the dynamics of labeled constructs leaking into and washing out of tumors [10, 46, 47, 51, 61, 88].

In the evaluation of contrast agent dynamics from MRI images, the arterial input function as well as nonlinear effects of agent concentration must be determined. Particularly in small animals, due to the rapid dissemination of the contrast agent bolus, such calculations can be challenging and modeling of the arterial input function is an attractive alternative. The most frequently used model for pharmacokinetic analysis of MRI data is based on a two-compartmental model with a central compartment representing the blood plasma and a tissue compartment representing the interstitial space of the tissue of interest [14, 107, 136]. The exchange constants between the central compartment and the tissue compartment can then be estimated and therefore the apparent permeability can be estimated.

Prior to the application of a pharmacokinetic model to dynamic MR data, we need to formulate a relationship between the time dependent contrast agent concentration and the measured MR signal. In kinetic studies of small brain metastases, we used a T1-weighted sequence (parameters below) with lower temporal resolution in favor of higher spatial resolution to resolve the small lesions. Due to the high initial contrast agent concentration, we chose to include the additional transverse decay term in our approximation of the signal:

$$S(t)=S_0(1-e^{-TR\cdot R_1})e^{-TE\cdot R_2} \quad (13)$$

where S_0 is a constant, TR is the repetition time, TE is the echo time, R_1 and R_2 are the longitudinal and transverse relaxation rates, respectively. The measured MR signal depends on the relaxation rates (R_1 and R_2). Both R_1 and R_2 are functions of contrast agent concentration as well as base relaxation rates (relaxation rate of the material in the absence of contrast agent) R_{10} and R_{20}. The measured longitudinal relaxation rate, R_1, is often approximated as having a linear dependence on contrast agent concentration:

$$R_1=R_{10}+r_1*C_B \quad (14)$$

where R_{10} is the longitudinal relaxation rate of tissue in the absence of the contrast agent, R_1 is the measured longitudinal relaxation rate, r_1 is the molar longitudinal relaxivity, and C_B is the concentration of the contrast agent in the blood. In our studies, we have observed a linear relationship between Gd-HPDO3A (ProHance) concentration and R_1 in *ex vivo* mouse blood, obtaining values of R_{10} = 0.5051 s^{-1}, r_1 = 3.904 mM/sec from a standard saturation recovery experiment. Similar to R_1, the transverse relaxivity, R_2, is often approximated as linear over some concentration regimes but has been previously reported to exhibit a 2nd order relationship with contrast agent concentration at high field strength [12]. Indeed, similar to Blockley et al, we found, via a multiple echo experiment, that the transverse relaxation rate dependence on Gd-HPDO3A concentration in *ex vivo* mouse blood could only be properly represented by a quadratic fit (Fig. 6A (bottom)):

$$R_2=R_{20}+\alpha^*C_B+\beta^*{C_B}^2 \quad (15)$$

where R_{20} is the transverse relaxation rate of mouse blood in the absence of contrast agent. The results for Gd-HPDO3A in whole mouse blood gave values of R_{20} =113.4 s^{-1}, α = −16.22 mM/sec and β = 4.479 mM^2/sec. From Eqs. 13 – 15, we can determine the relationship (following a 90° RF pulse) between the time dependent contrast agent concentration in the blood, $C_B(t)$, and the measured MR signal at that same point in time, $S(t)$:

$$S(t)=S_0(1-e^{-TR(R_{10}+r_1C_B(t))})e^{-TE(R_{20}+\alpha C_B(t)+\beta C_B^2(t))} \quad (16)$$

As an example, we evaluated apparent permeability in a model of brain metastasis at high field [102]. All *in vivo* studies were approved by the UC Davis Animal Care and Use Committee. In this model system, human melanoma cells were injected into the left cardiac ventricle. The use of high field MRI (7T Biospec 70/30, Bruker BioSpin MRI, Ettlingen, Germany) allowed us for the first time to evaluate apparent permeability within small metastatic lesions. Relevant parameters include a BGA-12S gradient coil, linearly polarized 72 mm I.D. resonator, four channel receive only phased array surface coil, T1w brain imaging (2D RARE,ETL = 2, TR/TE = 350 ms/9 ms, 14 repetitions, SI/ST = 1 mm/1 mm, 6 images, FOV = 2 × 2 cm, matrix = 256 × 192, NA = 5). The T1w signal was evaluated in regions of interest and signal intensity data was then converted to contrast agent concentration in the corresponding regions according to Eq. 16 via a non-linear fit in MATLAB (v2011a, MathWorks, Inc., Natick, MA). The parameters R_{10}, r_1, R_{20}, α, β were derived from *ex vivo* experiments as outlined above. S_0 was determined from the pre-injection signal for each animal.

As noted above, r_2 increases substantially for contrast agents at high field, which causes the non-linear dependence of the MR signal with contrast agent concentration to be exhibited at shorter echo times and lower contrast agent concentrations (Fig. 6a (top)). Thus, even with adequate temporal resolution, extracting the early phase of the kinetics curve may still be challenging. However, reasonable estimates of the true concentration versus time curve can be determined by either using a low concentration of contrast agent (and thus remaining in a mostly linear regime) or making corrections to the measured signal to partially compensate for R_2 effects. The former method is most easily implemented but may not provide a realistic description of most contrast enhanced MR studies, which often use bolus contrast agent concentrations well in excess of those necessary to ensure signal linearity.

In this study, we used a bolus concentration of 100 mM Gd-HPDO3A (0.5 μmol/g body weight total dose) and acquired a series of T1w images (Fig. 6b). The T1w signal intensity was then measured in brain arteries and metastatic tumors (Fig. 6c–d). The high bolus concentration, combined with the low tumor contrast agent concentration, result in a wide range of contrast agent concentrations of interest. Thus, neither a high nor low concentration approximation could be used. Therefore, the MATLAB nonlinear filling algorithm, nlinfit, was used to extract the time dependent contrast agent concentration from the measured MR signal (Fig. 6c–e) via Eq. 16.

The agent accumulates in the tumor and on average the T1 weighted-signal peaked at 168 seconds after injection. Based on five mice examined with an average of 5.2 and 18.6 regions of interest for brain arteries and metastatic tumors, respectively, the average apparent permeability of Gd-HPDO3A into and out of small metastatic tumors was then estimated as (1.1±0.2) $\times 10^{-6}$ and (2.37±0.2) $\times 10^{-5}$ cm/s. This apparent permeability is orders of magnitude larger than the apparent permeability of the larger albumin and liposomal tracers described in fully developed tumors in the previous section.

Imaging of the cargo release or internalization by target cells

As noted earlier, the uptake and intracellular trafficking of nanoparticles and their cargo can also be quantified with imaging techniques. With a combination of MRI contrast mechanisms, intracellular trafficking of liposomes following intra-tumoral injection has been evaluated and modeled [22]. The application of imaging to detect release of particle

cargo using MRI has also been accomplished with thermally activated particles [84, 111]. Quantitative kinetics of particles and their cargo with optical imaging has also been applied frequently to assess cargo stability and internalization [58, 77, 131].

Future

The future of image-guided interventions in general and image-guided drug delivery in particular appears to be very bright. The development of systems combining MRI with PET or with ultrasound not only facilitate treatment under imaging guidance, they can be used for the assessment of drug delivery to individual patients in challenging applications such as disorders of the central nervous system and for the pre-clinical optimization of nanodrug formulations for circulation stability and activation [5, 18, 32, 52, 56, 72]. Developments in positron emission tomography, such as the creation of scanners with an extended field of view, have the potential to greatly reduce the amount of material injected to acquire a pharmacokinetic scan and should enable studies of pharmacokinetics in human subjects [85]. The creation and optimization of hybrid MRI-ultrasound systems also facilitates the release of drug within a lesion and the *in vivo* assessment of delivery [32].

Pharmacokinetic models for nanotherapeutics will continue to evolve as the imaging technologies and the therapeutics themselves advance. Here, we demonstrated the application of apparent permeability to assess accumulation within a developing cancer, following ultrasound intervention and within small (100 micron) brain metastases. Such quantitative methodologies, used in partnership with new technologies, will provide a direct indication of the success of a therapeutic delivery strategy.

Acknowledgments

The authors acknowledge the support of NIHR01CA134549, NIHR01CA112356, NIHR01CA103828, T32EB003827 and the National Heart Lung and Blood Institute of the NIH as a Program of Excellence in Nanotechnology award (HHSN268201000043C).

References

1. Abou DS, Thorek DL, Ramos NN, Pinkse MW, Wolterbeek HT, Carlin SD, Beattie BJ, Lewis JS. ^{89}Zr-labeled paramagnetic octreotide-liposomes for PET-MR imaging of cancer. Pharmaceutical research. 2013; 30:878–888. [PubMed: 23224977]
2. Ahmad MZ, Akhter S, Rahman Z, Akhter S, Anwar M, Mallik N, Ahmad FJ. Nanometric gold in cancer nanotechnology: current status and future prospect. J Pharm Pharmacol. 2013; 65:634–651. [PubMed: 23600380]
3. Ahmed M, Monsky WE, Girnun G, Lukyanov A, D'Ippolito G, Kruskal JB, Stuart KE, Torchilin VP, Goldberg SN. Radiofrequency thermal ablation sharply increases intratumoral liposomal doxorubicin accumulation and tumor coagulation. Cancer Research. 2003; 63:6327–6333. [PubMed: 14559820]
4. Alkilany AM, Lohse SE, Murphy CJ. The Gold Standard: Gold Nanoparticle Libraries To Understand the Nano-Bio Interface. Accounts Chem Res. 2013; 46:650–661.
5. Alkins R, Burgess A, Ganguly M, Francia G, Kerbel R, Wels WS, Hynynen K. Focused Ultrasound Delivers Targeted Immune Cells to Metastatic Brain Tumors. Cancer Research. 2013; 73:1892–1899. [PubMed: 23302230]
6. Andreopoulos D, Kasi L, Edmund Kim E, Diaz M, Yang DJ, Asimacopoulos PJ. Detection of acute postoperative mediastinitis in mice using ^{99m}Tc-liposomes. Investigative radiology. 2002; 37:435–439. [PubMed: 12138359]
7. Awasthi V, Goins B, Klipper R, Loredo R, Korvick D, Phillips WT. Imaging experimental osteomyelitis using radiolabeled liposomes. Journal of nuclear medicine : official publication, Society of Nuclear Medicine. 1998; 39:1089–1094.

8. Bale R, Widmann G. Navigated CT-guided interventions. Minimally Invasive Therapy & Allied Technologies. 2007; 16:196–204. [PubMed: 17763092]
9. Bao A, Goins B, Klipper R, Negrete G, Mahindaratne M, Phillips WT. A novel liposome radiolabeling method using ^{99m}Tc-"SNS/S" complexes: in vitro and in vivo evaluation. Journal of pharmaceutical sciences. 2003; 92:1893–1904. [PubMed: 12950007]
10. Barentsz JO, Berger-Hartog O, Witjes JA, Hulsbergen-van der Kaa C, Oosterhof GON, VanderLaak JAWM, Kondacki H, Ruijs SHJ. Evaluation of chemotherapy in advanced urinary bladder cancer with fast dynamic contrast-enhanced MR imaging. Radiology. 1998; 207:791–797. [PubMed: 9609906]
11. Bhattacharyya S, Kurdziel K, Wei L, Riffle L, Kaur G, Hill GC, Jacobs PM, Tatum JL, Doroshow JH, Kalen JD. Zirconium-89 labeled panitumumab: a potential immuno-PET probe for HER1-expressing carcinomas. Nuclear medicine and biology. 2013; 40:451–457. [PubMed: 23454247]
12. Blockley NP, Jiang L, Gardener AG, Ludman CN, Francis ST, Gowland PA. Field Strength Dependence of R(1) and R(2)* Relaxivities of Human Whole Blood to ProHance, Vasovist, and Deoxyhemoglobin. Magnetic Resonance in Medicine. 2008; 60:1313–1320. [PubMed: 19030165]
13. Boellaard R. Standards for PET Image Acquisition and Quantitative Data Analysis. Journal of Nuclear Medicine. 2009; 50:11s–20s. [PubMed: 19380405]
14. Brix G, Semmler W, Port R, Schad LR, Layer G, Lorenz WJ. Pharmacokinetic Parameters in Cns Gd-Dtpa Enhanced Mr Imaging. J Comput Assist Tomo. 1991; 15:621–628.
15. Chang AJ, De Silva RA, Lapi SE. Development and characterization of ^{89}Zr-labeled panitumumab for immuno-positron emission tomographic imaging of the epidermal growth factor receptor. Molecular imaging. 2013; 12:17–27. [PubMed: 23348788]
16. Chen X, Barkauskas KJ, Weinberg BD, Duerk JL, Abdul-Karim FW, Paul S, Saidel GM. Dynamics of MRI-guided thermal ablation of VX2 tumor in paraspinal muscle of rabbits. Ieee Transactions on Biomedical Engineering. 2008; 55:1004–1014. [PubMed: 18334392]
17. Cho H, Lai TC, Kwon GS. Poly(ethylene glycol)-block-poly(epsilon-caprolactone) micelles for combination drug delivery: evaluation of paclitaxel, cyclopamine and gossypol in intraperitoneal xenograft models of ovarian cancer. Journal of controlled release : official journal of the Controlled Release Society. 2013; 166:1–9. [PubMed: 23246471]
18. Cline HE, Hynynen K, Hardy CJ, Watkins RD, Schenck JF, Jolesz FA. MR temperature mapping of focused ultrasound surgery. Magnetic Resonance in Medicine. 1994; 31:628–636. [PubMed: 8057815]
19. Curry FRE, Rygh CB, Karlsen T, Wiig H, Adamson RH, Clark JF, Lin YC, Gassner B, Thorsen F, Moen I, Tenstad O, Kuhn M, Reed RK. Atrial natriuretic peptide modulation of albumin clearance and contrast agent permeability in mouse skeletal muscle and skin: role in regulation of plasma volume. J Physiol-London. 2010; 588:325–339. [PubMed: 19948658]
20. Dams ET, Reijnen MM, Oyen WJ, Boerman OC, Laverman P, Storm G, van der Meer JW, Corstens FH, van Goor H. Imaging experimental intraabdominal abscesses with ^{99m}Tc-PEG liposomes and 99mTc-HYNIC IgG. Annals of surgery. 1999; 229:551–557. [PubMed: 10203089]
21. Daniel MC, Astruc D. Gold nanoparticles: Assembly, supramolecular chemistry, quantum-size-related properties, and applications toward biology, catalysis, and nanotechnology. Chem Rev. 2004; 104:293–346. [PubMed: 14719978]
22. Delli Castelli D, Dastrù W, Terreno E, Cittadino E, Mainini F, Torres E, Spadaro M, Aime S. In vivo MRI multicontrast kinetic analysis of the uptake and intracellular trafficking of paramagnetically labeled liposomes. Journal of Controlled Release. 2010; 144:271–279. [PubMed: 20230865]
23. Deri MA, Zeglis BM, Francesconi LC, Lewis JS. PET imaging with ^{89}Zr: from radiochemistry to the clinic. Nuclear medicine and biology. 2013; 40:3–14. [PubMed: 22998840]
24. Desale SS, Cohen SM, Zhao Y, Kabanov AV, Bronich TK. Biodegradable hybrid polymer micelles for combination drug therapy in ovarian cancer. J Control Release. 2013; 171:339–348. [PubMed: 23665258]
25. Devoogdt N, Xavier C, Hernot S, Vaneycken I, D'Huyvetter M, De Vos J, Massa S, De Baetselier P, Caveliers V, Lahoutte T. Molecular imaging using Nanobodies: a case study. Methods in molecular biology (Clifton, NJ). 2012; 911:559–567.

26. Dewhirst MW, Vujaskovic Z, Jones E, Thrall D. Re-setting the biologic rationale for thermal therapy. International Journal of Hyperthermia. 2005; 21:779–790. [PubMed: 16338861]
27. Dong H, Dube N, Shu JY, Seo JW, Mahakian LM, Ferrara KW, Xu T. Long-circulating 15 nm micelles based on amphiphilic 3-helix peptide-PEG conjugates. ACS nano. 2012; 6:5320–5329. [PubMed: 22545944]
28. Dreher MR, Liu WG, Michelich CR, Dewhirst MW, Yuan F, Chilkoti A. Tumor vascular permeability, accumulation, and penetration of macromolecular drug carriers. Journal of the National Cancer Institute. 2006; 98:335–344. [PubMed: 16507830]
29. Epenetos AA, Snook D, Durbin H, Johnson PM, Taylor-Papadimitriou J. Limitations of Radiolabeled Monoclonal Antibodies for Localization of Human Neoplasms. Cancer Research. 1986; 46:3183–3191. [PubMed: 3516393]
30. Erlemann R, Reiser MF, Peters PE, Vasallo P, Nommensen B, Kusnierzglaz CR, Ritter J, Roessner A. Musculoskeletal Neoplasms - Static and Dynamic Gd-Dtpa Enhanced Mr Imaging. Radiology. 1989; 171:767–773. [PubMed: 2717749]
31. Erlemann R, Sciuk J, Bosse A, Ritter J, Kusnierzglaz CR, Peters PE, Wuisman P. Response of Osteosarcoma and Ewing Sarcoma to Preoperative Chemotherapy -Assessment with Dynamic and Static Mr Imaging and Skeletal Scintigraphy. Radiology. 1990; 175:791–796. [PubMed: 2188300]
32. Fite BZ, Liu Y, Kruse DE, Caskey CF, Walton JH, Lai CY, Mahakian LM, Larrat B, Dumont E, Ferrara KW. Magnetic resonance thermometry at 7T for real-time monitoring and correction of ultrasound induced mild hyperthermia. PLoS One. 2012; 7:e35509. [PubMed: 22536396]
33. Frenkel V. Ultrasound mediated delivery of drugs and genes to solid tumors. Adv Drug Deliver Rev. 2008; 60:1193–1208.
34. Fry FJ, Ades HW, Fry WJ. Production of reversible changes in the central nervous system by ultrasound. Science. 1958; 127:83–84. [PubMed: 13495483]
35. Fry WJ, Dunn F. Ultrasonic irradiation of the central nervous system at high sound levels. Journal of the Acoustical Society of America. 1956; 28:129–131.
36. Fry WJ V, Wulff J, Tucker D, Fry FJ. Physical factors involved in ultrasonically induced changes in living systems: Identification of non-temperature effects. Journal of the Acoustical Society of America. 1950; 22:867–876.
37. Gaber MH, Wu NZ, Hong K, Huang SK, Dewhirst MW, Papahadjopoulos D. Thermosensitive liposomes: extravasation and release of contents in tumor microvascular networks. Int J Radiat Oncol Biol Phys. 1996; 36:1177–1187. [PubMed: 8985041]
38. Gabizon A, Price DC, Huberty J, Bresalier RS, Papahadjopoulos D. Effect of Liposome Composition and Other Factors on the Targeting of Liposomes to Experimental-Tumors - Biodistribution and Imaging Studies. Cancer Research. 1990; 50:6371–6378. [PubMed: 1698120]
39. Gabizon A, Shmeeda H, Barenholz Y. Pharmacokinetics of Pegylated Liposomal Doxorubicin. Review of Animal and Human Studies Clinical Pharmacokinetics. 2003; 42:419–436.
40. Gagnon MKJ, Hausner SH, Marik J, Abbey CK, Marshall JF, Sutcliffe JL. High-throughput in vivo screening of targeted molecular imaging agents. Proceedings of the National Academy of Sciences. 2009; 106:17904–17909.
41. Goldberg SN, Ahmed M. Minimally invasive image-guided therapies for hepatocellular carcinoma. Journal of Clinical Gastroenterology. 2002; 35:S115–S129. [PubMed: 12394215]
42. Gore JC, Manning HC, Quarles CC, Waddell KW, Yankeelov TE. Magnetic resonance in the era of molecular imaging of cancer. Magn Reson Imaging. 2011; 29:587–600. [PubMed: 21524870]
43. Hackel BJ, Kimura RH, Miao Z, Liu H, Sathirachinda A, Cheng Z, Chin FT, Gambhir SS. ^{18}F-Fluorobenzoate-Labeled Cystine Knot Peptides for PET Imaging of Integrin alphavbeta6. J Nucl Med. 2013; 54:1101–1105. [PubMed: 23670900]
44. Hajitou A, Pasqualini R, Arap W. Vascular targeting: Recent advances and therapeutic perspectives. Trends in Cardiovascular Medicine. 2006; 16:80–88. [PubMed: 16546688]
45. Hausner SH, Carpenter RD, Bauer N, Sutcliffe JL. Evaluation of an integrin alphavbeta6-specific peptide labeled with [^{18}F]fluorine by copper-free, strain-promoted click chemistry. Nuclear medicine and biology. 2013; 40:233–239. [PubMed: 23265667]
46. Hawighorst H, Knapstein PG, Schaeffer U, Knopp MV, Brix G, Hoffman U, Zuna I, Essig M, vanKaick G. Pelvic lesions in patients with treated cervical carcinoma: Efficacy of

pharmacokinetic analysis of dynamic MR images in distinguishing recurrent tumors from benign conditions. Am J Roentgenol. 1996; 166:401–408. [PubMed: 8553955]

47. Hawighorst H, Knapstein PG, Weikel W, Knopp MV, Zuna I, Knof A, Brix G, Schaeffer U, Wilkens C, Schoenberg SO, Essig M, Vaupel P, vanKaick G. Angiogenesis of uterine cervical carcinoma: Characterization by pharmacokinetic magnetic resonance parameters and histological microvessel density with correlation to lymphatic involvement. Cancer Research. 1997; 57:4777–4786. [PubMed: 9354439]
48. Holland JP, Divilov V, Bander NH, Smith-Jones PM, Larson SM, Lewis JS. ^{89}Zr-DFO-J591 for immunoPET of prostate-specific membrane antigen expression in vivo. Journal of nuclear medicine : official publication, Society of Nuclear Medicine. 2010; 51:1293–1300.
49. Howseman AM, Bowtell RW. Functional magnetic resonance imaging: imaging techniques and contrast mechanisms. Philos T Roy Soc B. 1999; 354:1179–1194.
50. http://www.traxtal.com.
51. Hulka CA, Smith BL, Sgroi DC, Tan LJ, Edmister WB, Semple JP, Campbell T, Kopans DB, Brady TJ, Weisskoff RM. Benign and Malignant Breast-Lesions - Differentiation with Echo-Planar Mr-Imaging. Radiology. 1995; 197:33–38. [PubMed: 7568850]
52. Hynynen K, Darkazanli A, Unger E, Schenck JF. MRI-Guided noninvasive ultrasound surgery. Med Phys. 1993; 20:107–115. [PubMed: 8455489]
53. Jacobson O, Zhu L, Niu G, Weiss ID, Szajek LP, Ma Y, Sun X, Yan Y, Kiesewetter DO, Liu S, Chen X. MicroPET imaging of integrin alphavbeta3 expressing tumors using ^{89}Zr-RGD peptides. Molecular imaging and biology : MIB : the official publication of the Academy of Molecular Imaging. 2011; 13:1224–1233. [PubMed: 21161690]
54. Johnson RP, Jeong YI, John JV, Chung CW, Kang DH, Selvaraj M, Suh H, Kim I. Dual Stimuli-Responsive Poly(N-isopropylacrylamide)-b-poly(l-histidine) Chimeric Materials for the Controlled Delivery of Doxorubicin into Liver Carcinoma. Biomacromolecules. 2013; 14:1434–1443. [PubMed: 23627834]
55. Jones EL, Oleson JR, Prosnitz LR, Samulski TV, Vujaskovic Z, Yu DH, Sanders LL, Dewhirst MW. Randomized trial of hyperthermia and radiation for superficial tumors. Journal of Clinical Oncology. 2005; 23:3079–3085. [PubMed: 15860867]
56. Judenhofer MS, Cherry SR. Applications for Preclinical PET/MRI. Seminars in Nuclear Medicine. 2013; 43:19–29. [PubMed: 23178086]
57. Key J, Cooper C, Kim AY, Dhawan D, Knapp DW, Kim K, Park JH, Choi K, Kwon IC, Park K, Leary JF. In vivo NIRF and MR dual-modality imaging using glycol chitosan nanoparticles. Journal of Controlled Release. 2012; 163:249–255. [PubMed: 22902594]
58. Kheirolomoom A, Kruse DE, Qin S, Watson KE, Lai CY, Young LJT, Cardiff RD, Ferrara KW. Enhanced in vivo bioluminescence imaging using liposomal luciferin delivery system. Journal of Controlled Release. 2010; 141:128–136. [PubMed: 19748536]
59. Kim SM, Haider MA, Milosevic M, Yeung IW. A comparison of dynamic contrast-enhanced CT and MR imaging-derived measurements in patients with cervical cancer. Clin Physiol Funct Imaging. 2013; 33:150–161. [PubMed: 23383694]
60. Klibanov AL, Maruyama K, Torchilin VP, Huang L. Amphipathic polyethylene glycols effectively prolong the circulation time of liposomes. Febs Letters. 1990; 268:235–237. [PubMed: 2384160]
61. Knopp MV, Himmelhan N, Radeleff J, Junkermann H, Hess T, Sinn HP, Brix G. Comparison of quantification techniques for dynamic contrast enhancement MRI analyzed using MR mammography. Radiologe. 2002; 42:280–290. [PubMed: 12063736]
62. Langereis S, Keupp J, van Velthoven JLJ, de Roos IHC, Burdinski D, Pikkemaat JA, Gruell H. A Temperature-Sensitive Liposomal H-1 CEST and F-19 Contrast Agent for MR Image-Guided Drug Delivery. Journal of the American Chemical Society. 2009; 131:1380. [PubMed: 19173663]
63. Laverman P, Dams ET, Oyen WJ, Storm G, Koenders EB, Prevost R, van der Meer JW, Corstens FH, Boerman OC. A novel method to label liposomes with ^{99m}Tc by the hydrazino nicotinyl derivative. Journal of nuclear medicine : official publication, Society of Nuclear Medicine. 1999; 40:192–197.
64. Lee SY, Park HS, Lee KY, Kim HJ, Jeon YJ, Jang TW, Lee KH, Kim YC, Kim KS, Oh IJ, Kim SY. Paclitaxel-Loaded Polymeric Micelle (230 mg/m(2)) and Cisplatin (60 mg/m(2)) vs.

Paclitaxel (175 mg/m(2)) and Cisplatin (60 mg/m(2)) in Advanced Non-Small-Cell Lung Cancer: A Multicenter Randomized Phase IIB Trial. Clin Lung Cancer. 2013; 14:275–282. [PubMed: 23290819]

65. Lencioni R, Crocetti L. Image-guided thermal ablation of hepatocellular carcinoma. Critical Reviews in Oncology/Hematology. 2008; 66:200–207. [PubMed: 18304832]
66. Liu D, Overbey D, Watkinson LD, Smith CJ, Daibes-Figueroa S, Hoffman TJ, Forte LR, Volkert WA, Giblin MF. Comparative evaluation of three ^{64}Cu-labeled E. coli heat-stable enterotoxin analogues for PET imaging of colorectal cancer. Bioconjug Chem. 2010; 21:1171–1176. [PubMed: 20536242]
67. Liu S, Hassink M, Selvaraj R, Yap LP, Park R, Wang H, Chen X, Fox JM, Li Z, Conti PS. Efficient ^{18}F labeling of cysteine-containing peptides and proteins using tetrazine-trans-cyclooctene ligation. Molecular imaging. 2013; 12:121–128. [PubMed: 23415400]
68. Logan J. Graphical analysis of PET data applied to reversible and irreversible tracers. Nuclear medicine and biology. 2000; 27:661–670. [PubMed: 11091109]
69. Lynn JG, Zwemer RL, Chick AJ, Miller AE. A new method for the generation and use of focused ultrasound in experimental biology. Jour Gen Physiol. 1942; 26:179–193. [PubMed: 19873337]
70. Marik J, Tartis MS, Zhang H, Fung JY, Kheirolomoom A, Sutcliffe JL, Ferrara KW. Long-circulating liposomes radiolabeled with [^{18}F]fluorodipalmitin ([^{18}F]FDP). Nuclear medicine and biology. 2007; 34:165–171. [PubMed: 17307124]
71. Meijs WE, Herscheid JD, Haisma HJ, Pinedo HM. Evaluation of desferal as a bifunctional chelating agent for labeling antibodies with Zr-89. International journal of radiation applications and instrumentation Part A, Applied radiation and isotopes. 1992; 43:1443–1447.
72. Ng T, Bading JR, Park R, Sohi H, Procissi D, Colcher D, Conti PS, Cherry SR, Raubitschek AA, Jacobs RE. Quantitative, Simultaneous PET/MRI for Intratumoral Imaging with an MRI-Compatible PET Scanner. Journal of Nuclear Medicine. 2012; 53:1102–1109. [PubMed: 22661534]
73. Niemeyer CM. Nanoparticles, proteins, and nucleic acids: Biotechnology meets materials science. Angew Chem Int Edit. 2001; 40:4128–4158.
74. Ogihara-Umeda I, Sasaki T, Kojima S, Nishigori H. Optimal radiolabeled liposomes for tumor imaging. Journal of nuclear medicine : official publication, Society of Nuclear Medicine. 1996; 37:326–332.
75. Ogihara-Umeda I, Sasaki T, Toyama H, Oda K, Senda M, Nishigori H. Rapid diagnostic imaging of cancer using radiolabeled liposomes. Cancer detection and prevention. 1997; 21:490–496. [PubMed: 9398989]
76. Ogihara I, Kojima S, Jay M. Differential uptake of gallium-67-labeled liposomes between tumors and inflammatory lesions in rats. Journal of nuclear medicine : official publication, Society of Nuclear Medicine. 1986; 27:1300–1307.
77. Paoli EE, Kruse DE, Seo JW, Zhang H, Kheirolomoom A, Watson KD, Chiu P, Stahlberg H, Ferrara KW. An optical and microPET assessment of thermally-sensitive liposome biodistribution in the Met-1 tumor model: Importance of formulation. Journal of Controlled Release. 2010; 143:13–22. [PubMed: 20006659]
78. Parker DL. Applications of Nmr Imaging in Hyperthermia - an Evaluation of the Potential for Localized Tissue Heating and Noninvasive Temperature Monitoring. Ieee Transactions on Biomedical Engineering. 1984; 31:161–167. [PubMed: 6724602]
79. Parker DL, Smith V, Sheldon P, Crooks LE, Fussell L. Temperature Distribution Measurements in Two-Dimensional Nmr Imaging. Med Phys. 1983; 10:321–325. [PubMed: 6877179]
80. Perrault SD, Walkey C, Jennings T, Fischer HC, Chan WCW. Mediating Tumor Targeting Efficiency of Nanoparticles Through Design. Nano Lett. 2009; 9:1909–1915. [PubMed: 19344179]
81. Persson M, Liu H, Madsen J, Cheng Z, Kjaer A. First ^{18}F-labeled ligand for PET imaging of uPAR: in vivo studies in human prostate cancer xenografts. Nucl Med Biol. 2013; 40:618–624. [PubMed: 23602763]
82. Peters RD, Hinks RS, Henkelman RM. Ex vivo tissue-type independence in proton-resonance frequency shift MR thermometry. Magn Reson Med. 1998; 40:454–459. [PubMed: 9727949]

83. Phillips WT, Rudolph AS, Goins B, Timmons JH, Klipper R, Blumhardt R. A simple method for producing a technetium-99m-labeled liposome which is stable in vivo. International journal of radiation applications and instrumentation. 1992; 19:539–547.
84. Ponce AM, Viglianti BL, Yu DH, Yarmolenko PS, Michelich CR, Woo J, Bally MB, Dewhirst MW. Magnetic resonance imaging of temperature-sensitive liposome release: Drug dose painting and antitumor effects. Journal of the National Cancer Institute. 2007; 99:53–63. [PubMed: 17202113]
85. Poon J, Dahlbom M, Moses W, Balakrishnan K, Wang W, Cherry S, Badawi R. Optimal whole-body PET scanner configurations for different volumes of LSO scintillator: a simulation study. Physics in Medicine and Biology. 2012; 57:4077. [PubMed: 22678106]
86. Qin S, Seo JW, Zhang H, Qi J, Curry FR, Ferrara KW. An imaging-driven model for liposomal stability and circulation. Molecular pharmaceutics. 2010; 7:12–21. [PubMed: 19621944]
87. Quesson B, de Zwart JA, Moonen CTW. Magnetic resonance temperature imaging for guidance of thermotherapy. J Magn Reson Imaging. 2000; 12:525–533. [PubMed: 11042633]
88. Reddick WE, Bhargava R, Taylor JS, Meyer WH, Fletcher BD. Dynamic contrast-enhanced MR imaging evaluation of osteosarcoma response to neoadjuvant chemotherapy. J Magn Reson Imaging. 1995; 5:689–694. [PubMed: 8748487]
89. Rieke V, Butts Pauly K. MR thermometry. J Magn Reson Imaging. 2008; 27:376–390. [PubMed: 18219673]
90. Roemer RB. Engineering aspects of hyperthermia therapy. Annual Review of Biomedical Engineering. 1999; 1:347–376.
91. Rossin R, Pan D, Qi K, Turner JL, Sun X, Wooley KL, Welch MJ. 64Cu-labeled folate-conjugated shell cross-linked nanoparticles for tumor imaging and radiotherapy: synthesis, radiolabeling, and biologic evaluation. Journal of nuclear medicine : official publication, Society of Nuclear Medicine. 2005; 46:1210–1218.
92. Rybak J, Trachsel E, Scheuermann J, Neri D. Ligand-Based Vascular Targeting of Disease. Chem Med Chem. 2007; 2:22–40. [PubMed: 17154429]
93. Rygh CB, Qin S, Seo JW, Mahakian LM, Zhang H, Adamson R, Chen JQ, Borowsky AD, Cardiff RD, Reed RK, Curry FR, Ferrara KW. Longitudinal investigation of permeability and distribution of macromolecules in mouse malignant transformation using PET. Clinical cancer research : an official journal of the American Association for Cancer Research. 2011; 17:550–559. [PubMed: 21106723]
94. Schoonooghe S, Laoui D, Van Ginderachter JA, Devoogdt N, Lahoutte T, De Baetselier P, Raes G. Novel applications of nanobodies for in vivo bio-imaging of inflamed tissues in inflammatory diseases and cancer. Immunobiology. 2012; 217:1266–1272. [PubMed: 22884356]
95. Sedlacek, HH.; Seeman, G.; Hoffman, D.; Czech; Lorenz, P.; Kolar, C.; Bossler, K. Contributions to Oncology. 1St. S Karger Publishing; NEW YORK, USA: 1992. Antibodies as carriers of cytotoxicity; p. 74-75.(May 7, 1992)
96. Seo JW, Mahakian LM, Kheirolomoom A, Zhang H, Meares CF, Ferdani R, Anderson CJ, Ferrara KW. Liposomal Cu-64 Labeling Method Using Bifunctional Chelators: Poly(ethylene glycol) Spacer and Chelator Effects. Bioconjugate Chemistry. 2010; 21:1206–1215. [PubMed: 20568726]
97. Seo JW, Zhang H, Kukis D, Meares C, Ferrara K. A Novel Method to Label Preformed Liposomes with Cu-64 for Positron Emission Tomography (PET) Imaging. Bioconjugate Chemistry. 2008; 19:2577–2584. [PubMed: 18991368]
98. Shokeen M, Anderson CJ. Molecular imaging of cancer with copper-64 radiopharmaceuticals and positron emission tomography (PET). Accounts of chemical research. 2009; 42:832–841. [PubMed: 19530674]
99. Shokeen M, Zheleznyak A, Wilson JM, Jiang M, Liu R, Ferdani R, Lam KS, Schwarz JK, Anderson CJ. Molecular imaging of very late antigen-4 (alpha4beta1 integrin) in the premetastatic niche. Journal of nuclear medicine : official publication, Society of Nuclear Medicine. 2012; 53:779–786.
100. Smith SV. Molecular imaging with copper-64. Journal of inorganic biochemistry. 2004; 98:1874–1901. [PubMed: 15522415]

101. Sugyo A, Tsuji AB, Sudo H, Nagatsu K, Koizumi M, Ukai Y, Kurosawa G, Zhang MR, Kurosawa Y, Saga T. Evaluation of ^{89}Zr-Labeled Human Anti-CD147 Monoclonal Antibody as a Positron Emission Tomography Probe in a Mouse Model of Pancreatic Cancer. PLoS One. 2013; 8:e61230. [PubMed: 23577210]
102. Sundstrøm T, Daphu I, Wendelbo I, Hodneland E, Lundervold A, Immervoll H, Skaftnesmo KO, Babic M, Jendelova P, Sykova E, Lund-Johansen M, Bjerkvig R, Thorsen F. Automated Tracking of Nanoparticle-labeled Melanoma Cells Improves the Predictive Power of a Brain Metastasis Model. Cancer Research. 2013; 73:2445–2456. [PubMed: 23423977]
103. Taylor JS, Reddick WE. Evolution from empirical dynamic contrast-enhanced magnetic resonance imaging to pharmacokinetic MRI. Adv Drug Deliver Rev. 2000; 41:91–110.
104. Terreno E, Castelli DD, Violante E, Sanders HMHF, Sommerdijk NAJM, Aime S. Osmotically Shrunken LIPOCEST Agents: An Innovative Class of Magnetic Resonance Imaging Contrast Media Based on Chemical Exchange Saturation Transfer. Chemistry. 2009; 15:1440–1448. [PubMed: 19115311]
105. Thaxton CS, Georganopoulou DG, Mirkin CA. Gold nanoparticle probes for the detection of nucleic acid targets. Clin Chim Acta. 2006; 363:120–126. [PubMed: 16214124]
106. Tofts PS, Brix G, Buckley DL, Evelhoch JL, Henderson E, Knopp M, Larsson HBW, Lee TY, Mayr NA, Parker GJM, Port RE, Taylor J, Weisskoff RM. Estimating kinetic parameters from dynamic contrast-enhanced T(1)-weighted MRI of a diffusable tracer: Standardized quantities and symbols. J Magn Reson Imaging. 1999; 10:223–232. [PubMed: 10508281]
107. Tofts PS, Kermode AG. Measurement of the Blood-Brain-Barrier Permeability and Leakage Space Using Dynamic Mr Imaging.1. Fundamental-Concepts. Magnetic Resonance in Medicine. 1991; 17:357–367. [PubMed: 2062210]
108. Tomasi G, Turkheimer F, Aboagye E. Importance of Quantification for the Analysis of PET Data in Oncology: Review of Current Methods and Trends for the Future. Molecular Imaging and Biology. 2012; 14:131–146. [PubMed: 21842339]
109. Tousoulis D, Antoniades C, Koumallos N, Marinou K, Stefanadi E, Latsios G, Stefanadis C. Novel Therapies Targeting Vascular Endothelium. Endothelium. 2006; 13:411– 421. [PubMed: 17169773]
110. Vallabhajosula S. ^{18}F-labeled positron emission tomographic radiopharmaceuticals in oncology: an overview of radiochemistry and mechanisms of tumor localization. Semin Nucl Med. 2007; 37:400–419. [PubMed: 17920348]
111. Viglianti BL, Abraham SA, Michelich CR, Yarmolenko PS, MacFall JR, Bally MB, Dewhirst MW. In vivo monitoring of tissue pharmacokinetics of liposome/drug using MRI: Illustration of targeted delivery. Magnetic Resonance in Medicine. 2004; 51:1153–1162. [PubMed: 15170835]
112. Vugts DJ, Visser GW, van Dongen GA. (89)Zr-PET Radiochemistry in the Development and Application of Therapeutic Monoclonal Antibodies and Other Biologicals. Current topics in medicinal chemistry. 2013; 13:446–457. [PubMed: 23432007]
113. Wadas TJ, Anderson CJ. Radiolabeling of TETA- and CB-TE2A-conjugated peptides with copper-64. Nature protocols. 2006; 1:3062–3068.
114. Wadas TJ, Wong EH, Weisman GR, Anderson CJ. Copper chelation chemistry and its role in copper radiopharmaceuticals. Current Pharmaceutical Design. 2007; 13:3–16. [PubMed: 17266585]
115. Wall PD, Fry WJ, Stephens R, Tucker D, Lettvin JY. Changes produced in the central nervous system by ultrasound. Science. 1951; 114:686–687. [PubMed: 14913137]
116. Wang S, Shin IS, Hancock H, Jang B-s, Kim H-s, Lee SM, Zderic V, Frenkel V, Pastan I, Paik CH, Dreher MR. Pulsed high intensity focused ultrasound increases penetration and therapeutic efficacy of monoclonal antibodies in murine xenograft tumors. Journal of Controlled Release. 2012; 162:218–224. [PubMed: 22732476]
117. Wang YF, Liu PF, Qiu LH, Sun Y, Zhu MJ, Gu LY, Di W, Duan YR. Toxicity and therapy of cisplatin-loaded EGF modified mPEG-PLGA-PLL nanoparticles for SKOV3 cancer in mice. Biomaterials. 2013; 34:4068–4077. [PubMed: 23480957]
118. Wang YX. Superparamagnetic iron oxide based MRI contrast agents: Current status of clinical application. Quant Imaging Med Surg. 2011; 1:35–40. [PubMed: 23256052]

119. Wang ZX, Ma LN. Gold nanoparticle probes. Coordin Chem Rev. 2009; 253:1607–1618.
120. Watson KD, Lai CY, Qin S, Kruse DE, Lin YC, Seo JW, Cardiff RD, Mahakian LM, Beegle J, Inghanm ES, Curry FR, Reed RK, Ferrara KW. Ultrasound increases nanoparticle delivery by reducing intratumoral pressure and increasing transport in epithelial and epithelial-mesenchymal transition tumors. Cancer Research. 2012; 72:1485–1493. [PubMed: 22282664]
121. Weber WA. Use of PET for monitoring cancer therapy and for predicting outcome. Journal of Nuclear Medicine. 2005; 46:983–995. [PubMed: 15937310]
122. Wei T, Liu J, Ma H, Cheng Q, Huang Y, Zhao J, Huo S, Xue X, Liang Z, Liang XJ. Functionalized nanoscale micelles improve drug delivery for cancer therapy in vitro and in vivo. Nano Lett. 2013; 13:2528–2534. [PubMed: 23634882]
123. Weinmann HJ, Laniado M, Mutzel W. Pharmacokinetics of Gddtpa Dimeglumine after Intravenous-Injection into Healthy-Volunteers. Physiol Chem Phys. 1984; 16:167–172.
124. White JB, Hausner SH, Carpenter RD, Sutcliffe JL. Optimization of the solid-phase synthesis of [^{18}F] radiolabeled peptides for positron emission tomography. Applied radiation and isotopes : including data, instrumentation and methods for use in agriculture, industry and medicine. 2012; 70:2720–2729.
125. Wong AW, Ormsby E, Zhang H, Seo JW, Mahakian LM, Caskey CF, Ferrara KW. A comparison of image contrast with ^{64}Cu-labeled long circulating liposomes and ^{18}F-FDG in a murine model of mammary carcinoma. American journal of nuclear medicine and molecular imaging. 2013; 3:32–43. [PubMed: 23342299]
126. Wood BJ, Poon RT, Locklin JK, Dreher MR, Ng KK, Eugeni M, Seidel G, Dromi S, Neennan Z, Kolf M, Black CDV, Prabhakar R, Libutti SK. Phase I Study of Heat-Deployed Liposomal Doxorubicin during Radiofrequency Ablation for Hepatic Malignancies. Journal of Vascular and Interventional Radiology. 2012; 23:248–255. [PubMed: 22178041]
127. Woodle MC. ^{67}Gallium-labeled liposomes with prolonged circulation: preparation and potential as nuclear imaging agents. Nuclear medicine and biology. 1993; 20:149–155. [PubMed: 8448567]
128. Xiao Y, Hong H, Javadi A, Engle JW, Xu W, Yang Y, Zhang Y, Barnhart TE, Cai W, Gong S. Multifunctional unimolecular micelles for cancer-targeted drug delivery and positron emission tomography imaging. Biomaterials. 2012; 33:3071–3082. [PubMed: 22281424]
129. Xu W I, Siddiqui A, Nihal M, Pilla S, Rosenthal K, Mukhtar H, Gong S. Aptamer-conjugated and doxorubicin-loaded unimolecular micelles for targeted therapy of prostate cancer. Biomaterials. 2013; 34:5244–5253. [PubMed: 23582862]
130. Yap JT, Carney JPJ, Hall NC, Townsend DW. Image-guided cancer therapy using PET/CT. Cancer Journal. 2004; 10:221–233.
131. Yhee J, Kim S, Koo H, Son S, Ryu J, Youn I, Choi K, Kwon I, Kim K. Optical Imaging of Cancer-Related Proteases Using Near-Infrared Fluorescence Matrix Metalloproteinase-Sensitive and Cathepsin B-Sensitive Probes. Theranostics. 2012; 2:179–189. [PubMed: 22375156]
132. Zhang H, Kusunose J, Kheirolomoom A, Seo JW, Qi J, Watson KD, Lindfors HA, Ruoslahti E, Sutcliffe JL, Ferrara KW. Dynamic imaging of arginine-rich heart-targeted vehicles in a mouse model. Biomaterials. 2008; 29:1976–1988. [PubMed: 18255141]
133. Zhang H, Li N, Sirish P, Mahakian L, Ingham E, Curry FR, Yamada S, Chiamvimonvat N, Ferrara KW. The cargo of CRPPR-conjugated liposomes crosses the intact murine cardiac endothelium. Journal of controlled release : official journal of the Controlled Release Society. 2012; 163:10–17. [PubMed: 22776291]
134. Zhang, XX.; Sun, Z.; Guo, J.; Wang, Z.; Wu, C.; Niu, G.; Ma, Y.; Kiesewetter, DO.; Chen, X. Molecular imaging and biology : MIB : the official publication of the Academy of Molecular Imaging. 2013. Comparison of F-labeled CXCR4 antagonist peptides for PET imaging of CXCR4 expression.
135. Zhang Y, Hong H, Cai W. PET tracers based on Zirconium-89. Current radiopharmaceuticals. 2011; 4:131–139. [PubMed: 22191652]
136. Taxt T, Jiřík R, Rygh CB, Grüner R, Bartos M, Andersen E, Curry FR, Reed RK. Single-channel blind estimation of arterial input function and tissue impulse response in DCE-MRI. IEEE Trans Biomed Eng. 2012 Apr; 59(4):1012–21. [PubMed: 22217906]

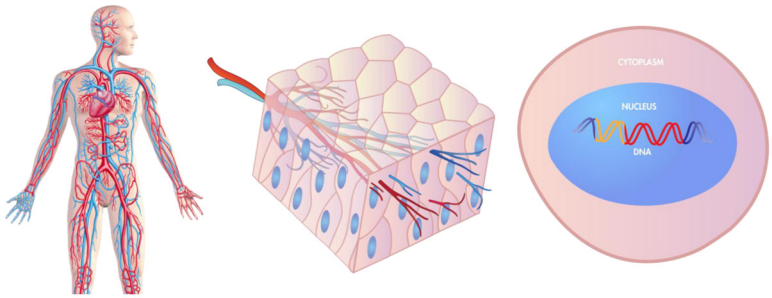

Figure 1. Therapeutics must cross barriers at the system (left), tissue (middle) and cellular (right) level

Imaging can assess the impact of barriers to nanoparticle delivery at each level and facilitate therapeutic optimization to enhance delivery. At the system level, therapeutics must be long circulating and must withstand serum degradation. Within tissues, drugs or carriers must extravasate and be transported to target cells. Finally, cellular internalization and trafficking is required for a subset of therapeutics to reach their target.

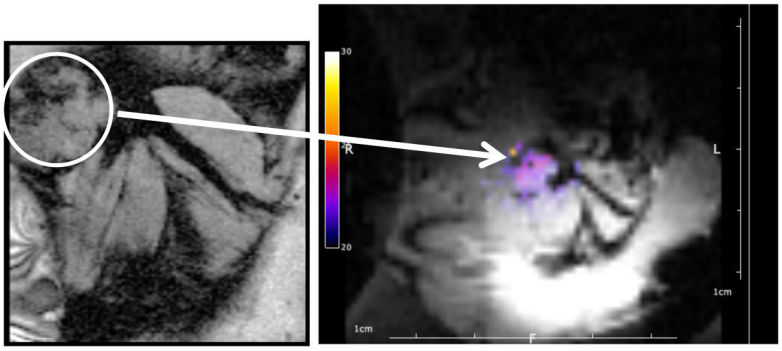

Figure 2. MR-guided focused ultrasound imaging facilitated temperature estimation within a mouse tumor model

Anatomical reference image (left) for localization of the tumor (white circle) prior to insonation. In this particular image, a syngeneic breast tumor was located in the mammary fat pad of a female FVB mouse. Note that position of the tumor in relation to the leg muscles on the image at the left. During insonation for mild hyperthermia, temperature data are acquired and overlaid on the MR magnitude image (right) and used for feedback control of the ultrasound.

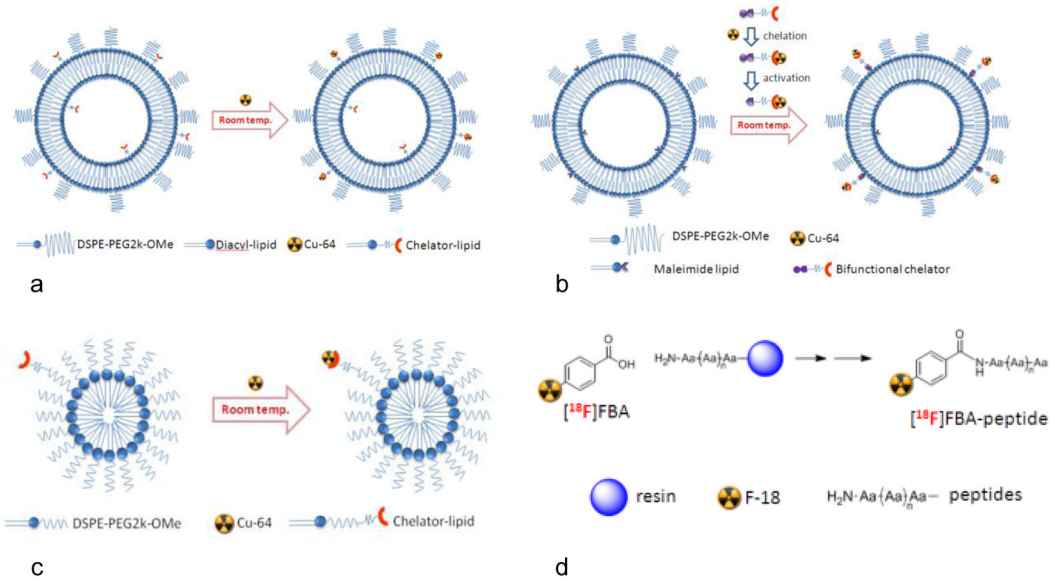

Figure 3. Approaches to radiolabeling

(a) Surface chelation of Cu-64 utilizing BAT-lipid. (b) Incorporation of Cu-64 via bifunctional chelator onto liposomal surface. (c) Radiolabeling micelles with Cu-64 via incorporated chelator-lipid (BAT-lipid). (d) Solid phase peptide radiolabeling with [^{18}F]FBA.

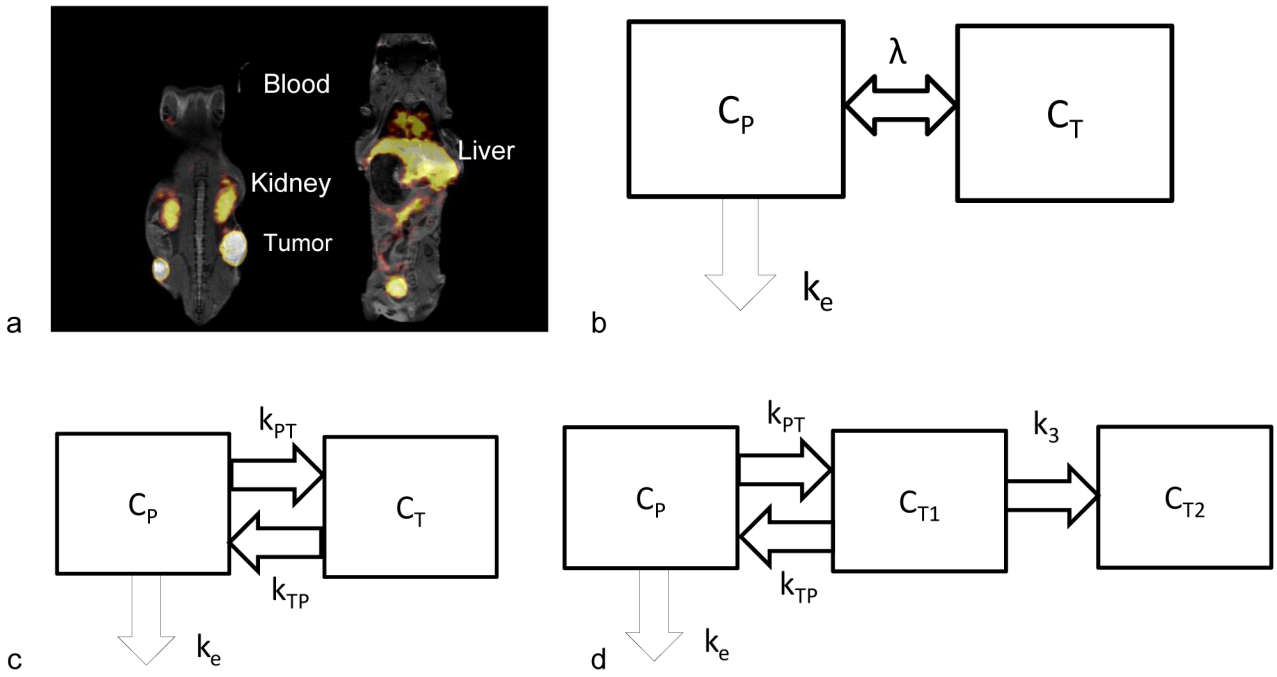

Figure 4. Imaging and compartmental modeling

(a) Examples (two planes) of an MR-PET fused image that can be applied to gain the anatomical reference from MRI with estimates of the tracer accumulation and clearance from PET. Here, radiolabeled particles are visible in the heart, liver, kidneys, bladder and tumors and regions of interest selection can be guided by the MRI image. (b) Two-compartment pharmacokinetic model (plasma and tumor) with a single bidirectional kinetic parameter. (c) Two-compartment pharmacokinetic model with uni-directional kinetic parameters. (d) Two-compartment pharmacokinetic model with uni-directional kinetic parameters and irreversible accumulation in tumor. Tumor compartment is composed of reversible C_{T1} and irreversible compartments C_{T2}. Diagrams adapted from [108].

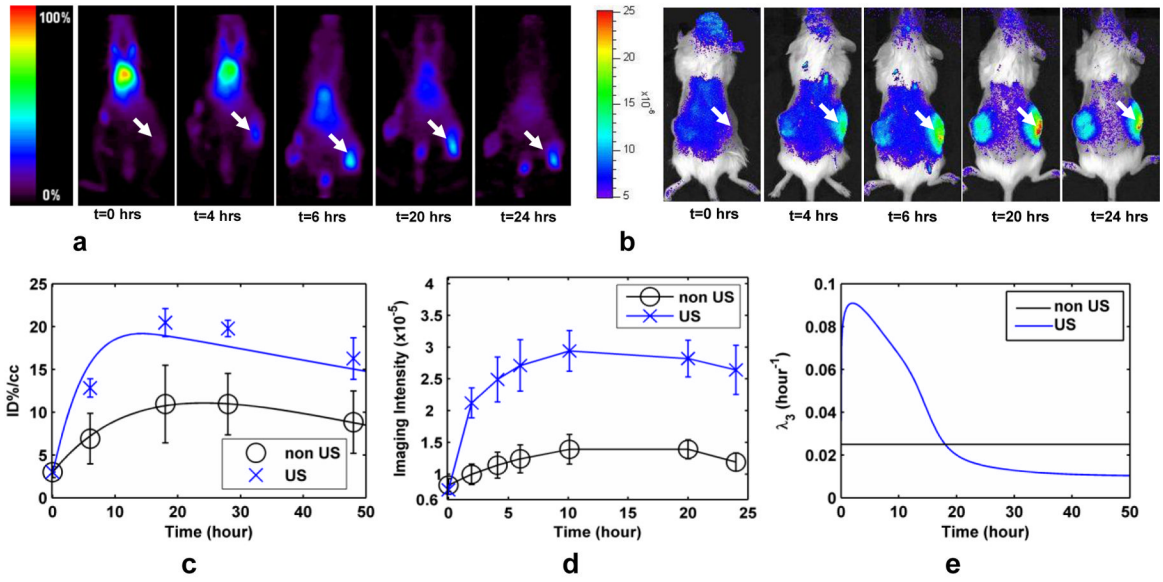

Figure 5. Effects of ultrasound on tumor accumulation of long circulating liposomes

(a) PET images of Met-1 syngeneic tumor acquired over 24 hours demonstrate the accumulation in an insonified, as compared with the contralateral, control tumor. White arrow indicates insonified tumor. (b) Optical images following systemic injection of dually-labeled (optical and PET) liposomes in Met-1 mouse tumor model demonstrating that the core and shell both accumulate within the tumor. (c) Time activity curve for positron emission tomography. (d) Fluorescence intensity from optical imaging studies of Met-1 tumor. (e) Time dependent transport rate, λ_3, resulting from insonation of Met-1 tumor.

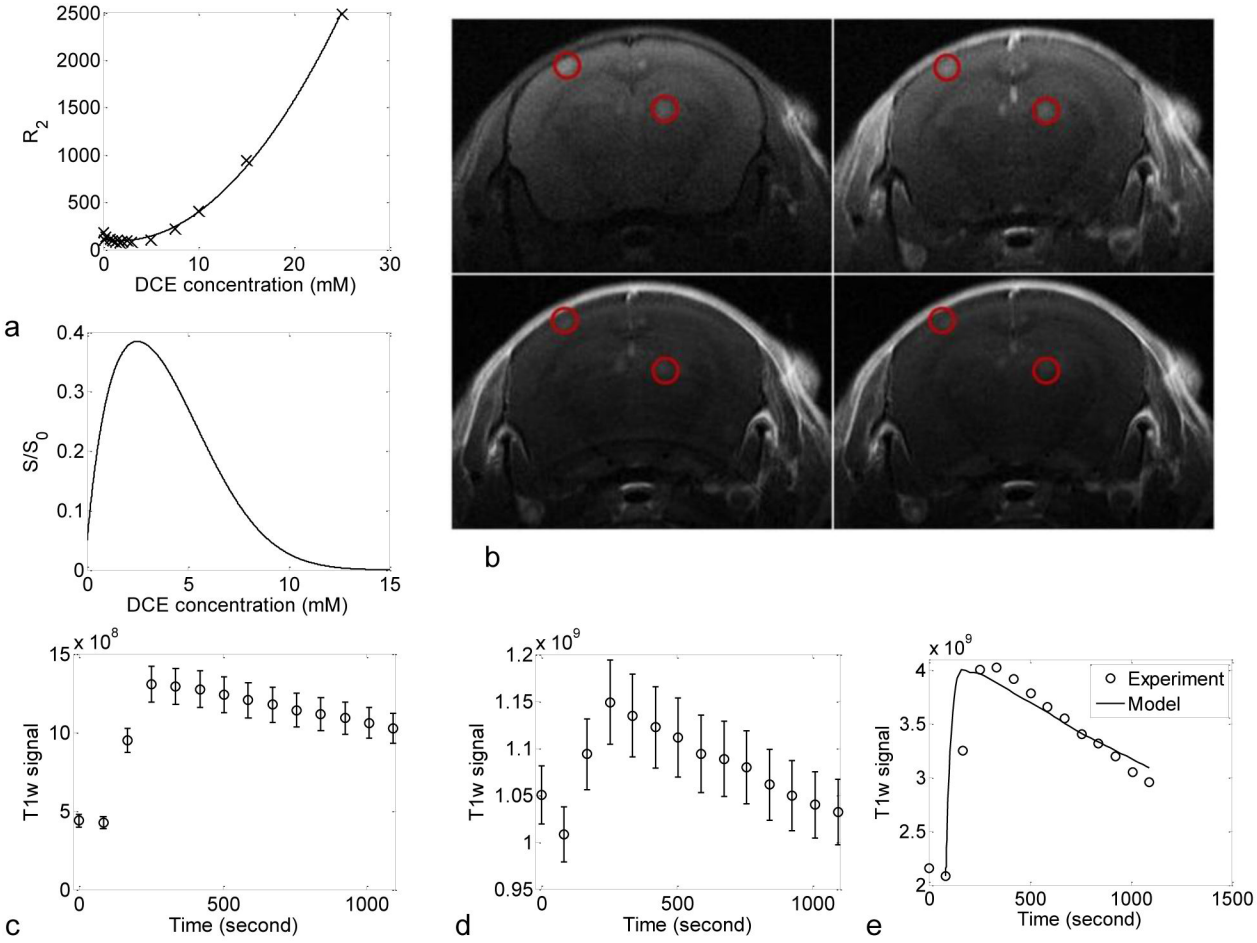

Figure 6. MRI in the evaluation of the extravasation of Gd-HPDO3A in 100 nm scale brain metastases

(a) (top) Experimentally measured (crossed lines) R_2 versus Gd-HPDO3A concentration in whole mouse blood *ex vivo* at 7T, and the quadratic fit (solid line) of the data. (bottom) The dependence of the (normalized) MR signal on Gd-HPDO3A concentration for the scan parameters used in our study. (b) Typical T1w kinetics MRI images at several time points (pre-injection, 84, 504, and 1008 seconds after injection). Red circles highlight small metastatic lesions. (c–e) Empty circles are experimental data and continuous lines are model prediction. (c) and (d) are averaged T1w signal in brain arteries and metastatic melanoma tumors: (c) in brain arteries, (d) tumors; (e) derived Gd-HPDO3A concentration in metastatic tumor. The error bars represent the standard error of the mean (SEM).

Table 1

Strengths and weaknesses of imaging modalities

	Sensitivity	Quantitation of carrier distribution and kinetics	Functional probes (e.g. molecular expression, blood flow, biochemistry)	Activatable probes (change properties due to caging, quenching, etc)
PET	Very high	Excellent	Many	None
MRI	Low	Limited applications	Some	Limited availability, can assess intracellular trafficking
Optical	Very high	Limited	Many	Many, can assess intracellular trafficking
Ultrasound	High	Limited applications	Blood flow /volume and molecular	Some

Table 2

Apparent permeability (AP) for albumin and liposomes in a mouse model of breast cancer in which the lesion progresses from a pre-cancer to invasive cancers between week 3 and 8 after implantation of the lesion [93].

Week	AP for liposomes imaged over the transition between ductal carcinoma in situ and invasive cancer ($\times 10^{-8}$cm/sec)	AP for albumin imaged over the transition between ductal carcinoma in situ and invasive cancer ($\times 10^{-8}$cm/sec)
3	0.5±0.4	2.1±0.4
5	0.5±0.2	2.6±0.9
7	1.2±0.3	5.4±0.9
8	1.3±0.3	6.6±1.6

Table 3

Apparent permeability (AP) for liposomes in mouse models of epithelial and epithelial-mesenchymal transition breast cancer [120].

Ultrasound	AP for liposomes in epithelial tumors ($\times 10^{-8}$cm/sec)	AP for liposomes in EMT tumors ($\times 10^{-8}$cm/sec)
No	4.1±2.8	2.7±1.4
Yes	6.7±4.6	5.1±3.6